

Large-eddy Simulation of Wall-bounded Turbulent Flow with High-order Discrete Unified Gas-Kinetic Scheme

Rui Zhang

Northwestern Polytechnical University

Chengwen Zhong (✉ zhongcw@nwpu.edu.cn)

<https://orcid.org/0000-0001-7664-437X>

Sha Liu

Northwestern Polytechnical University

Congshan Zhuo

Northwestern Polytechnical University

Research

Keywords: large-eddy simulation, wall-bounded turbulent flow, DUGKS, high order scheme

Posted Date: August 3rd, 2020

DOI: <https://doi.org/10.21203/rs.3.rs-50687/v1>

License:  This work is licensed under a Creative Commons Attribution 4.0 International License.

[Read Full License](#)

Version of Record: A version of this preprint was published on November 26th, 2020. See the published version at <https://doi.org/10.1186/s42774-020-00051-w>.

RESEARCH

Large-eddy Simulation of Wall-bounded Turbulent Flow with High-order Discrete Unified Gas-Kinetic Scheme

Rui Zhang¹, Chengwen Zhong^{1,2*}, Sha Liu^{1,2} and Congshan Zhuo^{1,2}

*Correspondence:

zhongcw@nwpu.edu.cn

¹School of Aeronautics,
Northwestern Polytechnical
University, 127 West Youyi Road,
710072, Xi'an, P.R.China
Full list of author information is
available at the end of the article

Abstract

In this paper, we introduce the incompressible discrete Maxwellian equilibrium distribution function and external forces into the two-stage third-order Discrete Unified Gas-Kinetic Scheme (DUGKS) for simulating low-speed incompressible turbulent flows with forcing term. The Wall-Adapting Local Eddy-viscosity (WALE) and Vreman sub-grid models for Large-Eddy Simulations (LES) of wall-bounded turbulent flows are coupled within the present framework. In order to simulate the three-dimensional turbulent flows associated with great computational cost, a parallel implementation strategy for the present framework is developed, and is validated by three canonical wall-bounded turbulent flows, viz., the fully developed turbulent channel flow at a friction Reynolds number (Re) about 180, the turbulent plane Couette flow at a friction Re number about 93 and three-dimensional lid-driven cubical cavity flow at a Re number of 12000. The turbulence statistics are computed by the present approach with both WALE and Vreman models, and their predictions match precisely with each other. Especially, the predicted flow physics of three-dimensional lid-driven cavity are consistent with the description from abundant literatures. While, they have small discrepancies in comparison to the Direct Numerical Simulation (DNS) due to the relatively low grid resolution. The present numerical results verify that the present two-stage third-order DUGKS-based LES method is capable for simulating inhomogeneous wall-bounded turbulent flows and getting reliable results with relatively coarse grids.

Keywords: large-eddy simulation; wall-bounded turbulent flow; DUGKS; high order scheme

1 Introduction

Turbulent flow is one of the most common and complicated problems in fluid dynamics. In the study of turbulent flows, they are usually formulated in terms of the Navier-Stokes (NS) equations for the macroscopic variables that are functions of position and time. Based on NS equations, many pioneers have successively proposed and applied the direct numerical simulation (DNS) [1, 2] approaches for numerical simulation of turbulence. Theoretically, DNS is designed to resolve all the scales of turbulent motion using very fine grid, which is unrivalled in accuracy and in the level of description provided [3], but the computational costs are very high, especially for high-Reynolds number turbulent flows. In order to balance the application and research requirements with the computational costs, the Reynolds averaged Navier-Stokes (RANS) methods [3, 4] have been developed and applied

on unresolved grids. The RANS method solves the time-averaged NS equations and the effect of the unsteady turbulent motions on the mean flow-field is approximated by turbulence models. Another alternative method, namely, the large-eddy simulation (LES) methods [5–7] have also attracted vast amount of attention of the engineering and scientific communities. The LES directly computes the large-scale turbulent structures and establishes a sub-grid scale (SGS) model to capture the effects of the smaller unresolved scales. Over the past several decades, the LES has become an indispensable fundamental research and engineering tool in the prediction and analysis of unsteady, multiscale, and multi-physics turbulent flows [8, 9].

The conventional approach for analyzing continuum physics is that uses a coarse-grained model in terms of macroscopic variables [10]. In recent years, some kinetic schemes based on the mesoscopic models have been utilized to simulate turbulent flows via combining with large-eddy simulation methods. Among them, because of the simplicity in formulation and multi-functionality, the lattice Boltzmann equation (LBE) methods has been widely and successfully used in the numerical simulation of turbulence. At present, the majority of the existing LBM-LES methods introduce the effect of eddy viscosity from SGS models into the relaxation time [11–13]. Hou et al. [14] firstly reported a simple large-eddy simulation based on LBM for two-dimensional turbulent flow. Premnath et al. [11] implemented both the standard Smagorinsky model [5] modified by using the van Driest wall-damping function and the dynamic procedure [15] to simulate a wall bounded turbulent flow. Recently, the wall-adapting local eddy-viscosity (WALE) model [16] and Vreman model [17] were reported within the lattice Boltzmann framework, such as multiple-relaxation time (MRT) [11, 12] and filter-matrix lattice Boltzmann (FMLB) [13] for simulating the fully developed turbulent channel flows. Besides, the gas-kinetic scheme (GKS) [18, 19] and implicit high-order GKS [20] for solving NS equations have also been extended to turbulent large-eddy simulations.

Recently, a discrete unified gas kinetic scheme (DUGKS) [21, 22] in a finite-volume framework has been developed, keeping the advantages of LBM, moreover, possessing a flexible mesh adaptation like unified gas kinetic scheme (UGKS) [23]. The characteristic difference solution of Boltzmann model equation, which couples the molecular advection and collision in numerical flux construction, makes the DUGKS be able to simulate the whole flow region from free molecular flow to continuum flow. In recent years, benefiting from the simulation capability of whole flow region, DUGKS has attracted vast amount of attention from the CFD communities in many scientific domains. Zhu et al. [24] extended the DUGKS to unstructured meshes. Wu et al. [25] proposed a DUGKS method considering the external force. An implicit DUGKS [26] for simulating of steady flow in all flow regions was constructed with an implicit macroscopic prediction technique [27]. Up to now, DUGKS has been applied to many fields, such as compressible flow [28, 29], multi-phase flow [30, 31], multi-component flow [32], complex motion (with immerse boundary method) [33], radiative transfer [34], etc.

DUGKS has also been used in direct numerical simulation of simple incompressible turbulent flows [35, 36], and another potential application of DUGKS is the large-eddy simulation of turbulent flows. Compared with the LBE method, the merits of DUGKS in turbulent simulation are better numerical stability and its support

for non-uniform and unstructured grids [24]. However, there are still some issues to be improved. For example, the DUGKS has a relatively large numerical dissipation compared with the LBE method [35], which is one of the reasons why the high-order DUGKS is needed for large-eddy simulation of turbulent flows. In addition, the LES for turbulent flows generally requires higher-order (greater than second) numerical methods to minimize the numerical error, because of the discretization error is dominant at all wave numbers for the second-order accurate scheme, whereas the sub-grid stress are dominant at the low frequencies for the high-order accurate scheme [8]. Recently, Wu et al. [37], inspired by two-stage fourth-order time accurate discretization (TFTD) method [38, 39], proposed a two-stage third-order DUGKS for low-speed isothermal flow by reducing the requirement of time accuracy. In this paper, for simulating low-speed incompressible flows, the incompressible discrete Maxwellian equilibrium distribution function [40, 41] is introduced to reduce the compressibility error. For the channel flow driven by external forces, the external force term is introduced into the high-order DUGKS. In addition, the distribution function will be approximated by the Taylor expansion with fourth-order accuracy.

The present work mainly focuses on combining the two-stage third-order DUGKS with the WALE model [16] and Vreman model [17] for large-eddy simulation of wall-bounded turbulent flows. The fully developed turbulent channel flow with a friction Reynolds number $Re_\tau = 180$, the turbulent plane Couette flow with a friction Reynolds number $Re_\tau = 93$ and the three-dimensional lid-driven cubical cavity flow with Reynolds number $Re = 12000$ were investigated to validate the capability and accuracy of the present high-order DUGKS (with D3Q19) for turbulent flows. The rest of this paper is organized as follows. In Section 2, the basic algorithm of two-stage third-order DUGKS with a force term is described, meanwhile, the key elements of LES-based DUGKS method and computation procedure are also given in Section 2. In Section 3, Three wall-bounded turbulent flow, respectively, the fully developed turbulent channel flow, the turbulent plane Couette flow and three-dimensional lid-driven cubical cavity flow were performed and discussed. Finally, conclusions and future outlook are given in Section 4.

2 Numerical method

2.1 Third-order DUGKS with force term

2.1.1 Two-stage third-order temporal discretization

The Boltzmann-BGK equation with a force term can be written as:

$$\frac{\partial f}{\partial t} = L(f) + \Omega(f) + S(f), \quad (1)$$

where $L(f)$, $\Omega(f)$, $S(f)$ are transport term, BGK collision operator [42] and external force term, respectively, which can be expressed as follows:

$$L(f) = -\boldsymbol{\xi} \cdot \nabla f, \quad (2)$$

$$\Omega(f) = \frac{f^{eq} - f}{\tau}, \quad (3)$$

$$S(f) = -\frac{\mathbf{F}}{\rho} \cdot \nabla_{\boldsymbol{\xi}} f, \quad (4)$$

where $f = f(\mathbf{x}, \boldsymbol{\xi}, t)$ is the distribution function which is defined as the density of particles at time t and in phase space $(\mathbf{x}, \boldsymbol{\xi})$. Here, \mathbf{x} is the physical space coordinates, $\boldsymbol{\xi}$ is the particle velocity. In Eq. (3), $\tau = \mu/p$ is the relaxation time where μ is the dynamic viscosity and p is the pressure, and f^{eq} is the Maxwellian equilibrium distribution function defined in the following form:

$$f^{eq} = \frac{\rho}{(2\pi RT)^{D/2}} \exp\left(-\frac{|\boldsymbol{\xi} - \mathbf{u}|^2}{2RT}\right), \quad (5)$$

where R is the specific gas constant, D is the spatial dimension, ρ is the density, \mathbf{u} is the macroscopic velocity of fluid, T is the temperature.

The conservative flow variables mass and momentum are considered in the low-speed isothermal flows and are defined as the moments of distribution function as follows:

$$\mathbf{W} = \begin{pmatrix} \rho \\ \rho\mathbf{u} \end{pmatrix} = \int \psi(\boldsymbol{\xi}) f d\boldsymbol{\xi}, \quad (6)$$

where $\psi(\boldsymbol{\xi}) = (1, \boldsymbol{\xi})^T$ are the collision invariants.

In Eq. (4), $\mathbf{F} = \mathbf{F}(\mathbf{x}, t)$ is external force per unit volume. According to Refs. [25, 43], the external force term $S(f)$ can be approximated as:

$$S(f) \approx -\frac{\mathbf{F}}{\rho} \cdot \nabla_{\boldsymbol{\xi}} f^{eq} = \frac{\mathbf{F} \cdot (\boldsymbol{\xi} - \mathbf{u})}{\rho RT} f^{eq} = \mathbf{H} f^{eq}, \quad (7)$$

where $\mathbf{H} = \frac{\mathbf{F} \cdot (\boldsymbol{\xi} - \mathbf{u})}{\rho RT}$.

For convenience in formula derivations, a new source term $Q(f)$ is defined as the summation of BGK collision operator and external force term:

$$Q(f) := \Omega(f) + S(f) = \frac{1}{\tau} [(1 + \mathbf{H}\tau) f^{eq} - f]. \quad (8)$$

Since the collision operator conserves mass and momentum, it is easy to verify that the source term $Q(f)$ satisfies the following conservative laws:

$$\int \psi(\boldsymbol{\xi}) Q(f) d\boldsymbol{\xi} = \begin{pmatrix} 0 \\ \mathbf{F} \end{pmatrix}. \quad (9)$$

Consequently, the Boltzmann-BGK equation with the force term can be rewritten as:

$$\frac{\partial f}{\partial t} = L(f) + Q(f). \quad (10)$$

The form of Eq. (10) is in accord with the Boltzmann-BGK equation without the force term which is used in the original two-stage third-order DUGKS [37], while

the only difference is that the original collision operator $\Omega(f)$ is replaced by a new source term $Q(f)$ including collision operator and force term.

The present third-order DUGKS algorithm with force term employs a finite-volume formulation. The flow domain is divided into a set of control volumes V_j centered at \mathbf{x}_j . Then integrating Eq. (10) in control volume V_j from time t_n to $t_n + \Delta t$ with third order time discretization method for transport term and source term same as third-order DUGKS [37]. Finally, the evolution equation Eq. (11) with third-order temporal accuracy can be obtained as follows:

$$\begin{aligned} f_j^{n+1} = & f_j^n + \frac{3}{4} \Delta t Q_j^{n+1/3} + \frac{1}{4} \Delta t Q_j^{n+1} + \frac{1}{7} \Delta t [3L_j^{n+1/6} + 4L_j^{n+3/4}] \\ & + O(\Delta t^4), \end{aligned} \quad (11)$$

where f_j and Q_j are the cell-averaged values of the distribution function and source term, e.g.,

$$f_j^{n+1} = \frac{1}{|V_j|} \int_{V_j} f(\mathbf{x}_j, \boldsymbol{\xi}, t_n + \Delta t) dV, \quad (12)$$

$$Q_j^{n+1/3} = \frac{1}{|V_j|} \int_{V_j} Q\left(\mathbf{x}_j, \boldsymbol{\xi}, t_n + \frac{1}{3} \Delta t\right) dV, \quad (13)$$

and $L_j^{n+1/6}$ and $L_j^{n+3/4}$ are the micro-fluxes across the interface of control volumes V_j :

$$L_j^{n+1/6} = \frac{1}{|V_j|} \int_{\partial V_j} (\boldsymbol{\xi} \cdot \mathbf{n}) f\left(\mathbf{x}_{cf}, \boldsymbol{\xi}, t_n + \frac{1}{6} \Delta t\right) dS, \quad (14)$$

$$L_j^{n+3/4} = \frac{1}{|V_j|} \int_{\partial V_j} (\boldsymbol{\xi} \cdot \mathbf{n}) f\left(\mathbf{x}_{cf}, \boldsymbol{\xi}, t_n + \frac{3}{4} \Delta t\right) dS, \quad (15)$$

where $|V_j|$ and ∂V_j are the volume and surface of control volumes V_j , \mathbf{n} is the outward unit normal vector on the surface, and \mathbf{x}_{cf} is the coordinates of point on this control surface (If the control surface is in discrete form, \mathbf{x}_{cf} is defined as the center of a discrete control surface). The time step Δt is determined by the Courant-Friedrichs-Lowy (CFL) condition and stability condition $\Delta t/\tau \leq 12$ [37]:

$$\Delta t = \min \left\{ C \frac{\Delta x_{\min}}{U_0 + \sqrt{3DRT}}, 12\tau \right\}, \quad (16)$$

where C is the CFL number, U_0 is the characteristic velocity of flow, and Δx_{\min} is the minimal grid spacing.

Like the original DUGKS [21, 37], in order to remove the implicit treatment of the source term Q_j^{n+1} in Eq. (11), a new auxiliary distribution function is introduced:

$$\hat{f}_j^{n+1} = f_j^{n+1} - \frac{\Delta t}{4} Q_j^{n+1}, \quad (17)$$

where the distribution function f can be expressed as follows from Eq. (17).

$$f = \frac{4\tau}{4\tau + \Delta t} \hat{f} + \frac{\Delta t}{4\tau + \Delta t} (1 + H\tau) f^{eq}. \quad (18)$$

Since the source term conserves mass and momentum, the following explicit evolution equation of the distribution function \hat{f} is solved instead of the original implicit one:

$$\hat{f}_j^{n+1} = f_j^n + \frac{3}{4} \Delta t Q_j^{n+1/3} + \frac{1}{7} \Delta t [3L_j^{n+1/6} + 4L_j^{n+3/4}], \quad (19)$$

and the conservative variables can be calculated from the auxiliary distribution function \hat{f}^{n+1} as follows:

$$\mathbf{W}^{n+1} = \begin{pmatrix} \rho \\ \rho u \end{pmatrix}^{n+1} = \int \psi(\xi) \hat{f} d\xi + \begin{pmatrix} 0 \\ \Delta t \mathbf{F}/4 \end{pmatrix}. \quad (20)$$

According to Eq. (19), it is necessary to evaluate source term $Q_j^{n+1/3}$ and micro-fluxes $L_j^{n+1/6}$ and $L_j^{n+3/4}$ in order to update the auxiliary distribution function. The calculation of the micro-fluxes will be described in the next section, and the second-order DUGKS method is used to update the source term $Q_j^{n+1/3}$. Integrating Eq. (10) in control volume V_j from t_n to $t_n + \Delta t/3$ with midpoint rule for the convection term and trapezoidal rule for the source term, it can be obtained that,

$$f_j^{n+1/3} - f_j^n + \frac{\Delta t}{3} L_j^{n+1/6} = \frac{\Delta t}{6} (Q_j^n + Q_j^{n+1/3}). \quad (21)$$

The following new set of auxiliary distribution functions are also introduced to remove the implicit terms in Eq. (21):

$$\tilde{f}_j^{n+1/3} = f_j^{n+1/3} - \frac{1}{6} \Delta t Q_j^{n+1/3}, \quad (22)$$

$$\tilde{f}_j^{+,n} = f_j^n + \frac{1}{6} \Delta t Q_j^n. \quad (23)$$

Then, Eq. (21) can be rewritten as:

$$\tilde{f}_j^{n+1/3} = \tilde{f}_j^{+,n} - \frac{\Delta t}{3} L_j^{n+1/6}. \quad (24)$$

The relations between auxiliary distribution functions \tilde{f} , \tilde{f}^+ and distribution functions f , \hat{f} are as follows:

$$f_j^{n+1/3} = \frac{6\tau}{6\tau + \Delta t} \tilde{f}_j^{n+1/3} + \frac{\Delta t}{6\tau + \Delta t} (1 + H\tau)_j^{n+1/3} f_j^{eq,n+1/3}, \quad (25)$$

$$f_j^n = \frac{6\tau}{6\tau - \Delta t} \tilde{f}_j^{+,n} - \frac{\Delta t}{6\tau - \Delta t} (1 + H\tau)_j^n f_j^{eq,n}, \quad (26)$$

$$\tilde{f}_j^{+,n} = \frac{12\tau - 2\Delta t}{12\tau + 3\Delta t} \hat{f}_j^n + \frac{5\Delta t}{12\tau + 3\Delta t} (1 + H\tau)_j^n f_j^{eq,n}. \quad (27)$$

The hydrodynamic variables density and fluid macroscopic velocity can be solved from the following equation (Eq. (28)), once the auxiliary distribution functions \tilde{f} at time $t_n + \Delta t/3$ is obtained.

$$\mathbf{W}^{n+1/3} = \begin{pmatrix} \rho \\ \rho \mathbf{u} \end{pmatrix}^{n+1/3} = \int \boldsymbol{\psi}(\boldsymbol{\xi}) \tilde{f} d\boldsymbol{\xi} + \begin{pmatrix} 0 \\ \Delta t \mathbf{F}/6 \end{pmatrix}, \quad (28)$$

meanwhile, $Q_j^{n+1/3}$ can also be obtained as follows:

$$\begin{aligned} Q_j^{n+1/3} &= \frac{1}{\tau} \left[(1 + H\tau)_j^{n+1/3} f_j^{eq,n+1/3} - f_j^{n+1/3} \right] \\ &= \frac{6\Delta t}{6\tau + \Delta t} \left[(1 + H\tau)_j^{n+1/3} f_j^{eq,n+1/3} - \tilde{f}_j^{n+1/3} \right]. \end{aligned} \quad (29)$$

2.1.2 Flux evaluation

According to Eq. (14) and Eq. (15), the key point in solving micro-fluxes $L_j^{n+1/6}$ and $L_j^{n+3/4}$ are calculating the distribution function $f(\mathbf{x}_{cf}, \boldsymbol{\xi}, t_n + \Delta t/6)$ and $f(\mathbf{x}_{cf}, \boldsymbol{\xi}, t_n + 3\Delta t/4)$ on the control surface. First, the Boltzmann-BGK equation in Eq. (10) is integrated within a half time step h along the characteristic line $\mathbf{x} + \boldsymbol{\xi}t$ whose end point \mathbf{x}_{cf} is located at the cell interface, which leads to the following characteristic line solution:

$$\begin{aligned} f(\mathbf{x}_{cf}, \boldsymbol{\xi}, t_* + h) - f(\mathbf{x}_{cf} - \boldsymbol{\xi}h, \boldsymbol{\xi}, t_*) \\ = \frac{h}{2} [Q(\mathbf{x}_{cf}, \boldsymbol{\xi}, t_* + h) + Q(\mathbf{x}_{cf} - \boldsymbol{\xi}h, \boldsymbol{\xi}, t_*)]. \end{aligned} \quad (30)$$

where $t_* = t_n$, $h = \Delta t/6$ and $t_* = t_n + \Delta t/3$, $h = 5\Delta t/12$ can be chosen for calculating $f(\mathbf{x}_{cf}, \boldsymbol{\xi}, t_n + \Delta t/6)$ and $f(\mathbf{x}_{cf}, \boldsymbol{\xi}, t_n + 3\Delta t/4)$, respectively. Similar to the treatment in Eq. (11), another auxiliary distribution function \bar{f} is introduced as follows to remove the implicit term in Eq. (30):

$$\bar{f} = f - \frac{h}{2} Q, \quad (31)$$

$$\bar{f}^+ = f + \frac{h}{2} Q. \quad (32)$$

Then Eq. (30) can be expressed as,

$$\bar{f}(\mathbf{x}_{cf}, \boldsymbol{\xi}, t_* + h) = \bar{f}^+(\mathbf{x}_{cf} - \boldsymbol{\xi}h, \boldsymbol{\xi}, t_*). \quad (33)$$

where the relationship between f and \bar{f} is:

$$\begin{aligned} f(\mathbf{x}_{cf}, \boldsymbol{\xi}, t_* + h) &= \frac{2\tau}{2\tau + h} \bar{f}(\mathbf{x}_{cf}, \boldsymbol{\xi}, t_* + h) \\ &\quad + \frac{h}{2\tau + h} (1 + H\tau) f^{eq}(\mathbf{x}_{cf}, \boldsymbol{\xi}, t_* + h). \end{aligned} \quad (34)$$

The distribution function $\bar{f}^+(\mathbf{x}_{cf} - \boldsymbol{\xi}h, \boldsymbol{\xi}, t_*)$ was approximated by second-order Taylor expansion in original third-order DUGKS. In present work, the distribution function $\bar{f}^+(\mathbf{x}_{cf} - \boldsymbol{\xi}h, \boldsymbol{\xi}, t_*)$ is approximated by the following third-order Taylor expansion to improve the spatial accuracy:

$$\begin{aligned} & \bar{f}^+(\mathbf{x}_{cf} - \xi_x h, y_{cf} - \xi_y h, z_{cf} - \xi_z h, \boldsymbol{\xi}, t_*) \\ &= \bar{f}^+(\mathbf{x}_c, y_c, z_c, \boldsymbol{\xi}, t_*) + \left(m \frac{\partial}{\partial x} + n \frac{\partial}{\partial y} + r \frac{\partial}{\partial z} \right) \bar{f}^+|_{\mathbf{x}_c, \boldsymbol{\xi}, t_*} \\ &+ \frac{1}{2} \left(m \frac{\partial}{\partial x} + n \frac{\partial}{\partial y} + r \frac{\partial}{\partial z} \right)^2 \bar{f}^+|_{\mathbf{x}_c, \boldsymbol{\xi}, t_*} + \frac{1}{6} \left(m \frac{\partial}{\partial x} + n \frac{\partial}{\partial y} + r \frac{\partial}{\partial z} \right)^3 \bar{f}^+|_{\mathbf{x}_c, \boldsymbol{\xi}, t_*} \\ &+ O(m^4 + n^4 + r^4), \quad \mathbf{x}_{cf} - \boldsymbol{\xi}h \in V_c. \end{aligned} \quad (35)$$

where the coefficients are $m = x_{cf} - \xi_x h - x_c$, $n = y_{cf} - \xi_y h - y_c$ and $r = z_{cf} - \xi_z h - z_c$. (x_c, y_c, z_c) and (x_{cf}, y_{cf}, z_{cf}) are the central points of cell and cell-interface, respectively. V_c is the cell whose center is located at (x_c, y_c, z_c) . All derivatives in Eq. (35) are calculated by the central difference method, where the p -order accuracy of central schemes used to approximate q -order derivatives should satisfy the relation $p + q \geq 4$.

The conservative variables at the control surfaces can be obtained by calculating the moments of the auxiliary distribution function \bar{f} with Eq. (36). Once the conservative variables at control surface are known, the equilibrium distribution function $f^{eq}(\mathbf{x}_{cf}, \boldsymbol{\xi}, t_* + h)$ can be obtained directly.

$$\begin{aligned} \rho(\mathbf{x}_{cf}, t_* + h) &= \int \bar{f}(\mathbf{x}_{cf}, \boldsymbol{\xi}, t_* + h) d\boldsymbol{\xi}, \\ \rho \mathbf{u}(\mathbf{x}_{cf}, t_* + h) &= \int \boldsymbol{\xi} \bar{f}(\mathbf{x}_{cf}, \boldsymbol{\xi}, t_* + h) d\boldsymbol{\xi} + \frac{h}{2} \mathbf{F}. \end{aligned} \quad (36)$$

Therefore, using Eqs. (35), (33), (36) and (34) in turn, the original distribution functions $f(\mathbf{x}_{cf}, \boldsymbol{\xi}, t_n + \Delta t/6)$ and $f(\mathbf{x}_{cf}, \boldsymbol{\xi}, t_n + 3\Delta t/4)$ can be obtained. With the determination of these original distribution functions, the micro-fluxes $L_j^{n+1/6}$ and $L_j^{n+3/4}$ can be fully evaluated according to Eq. (14) and Eq. (15). So far, the two-stage third-order DUGKS with external force is completely established, and the only remaining issue is the velocity space discretization.

2.2 Discrete velocity space

In the present two-stage third-order DUGKS, the Maxwellian equilibrium distribution f^{eq} is approximated by its second-order Taylor (or Hermit) expansion for the $Ma \ll 1$. By discretizing the velocity space and employing the Gauss-Hermite quadrature, the discrete equilibrium distribution function can be obtained,

$$f_\alpha^{eq} = \rho W_\alpha \left[1 + \frac{\boldsymbol{\xi}_\alpha \cdot \mathbf{u}}{RT} + \frac{1}{2} \left(\frac{\boldsymbol{\xi}_\alpha \cdot \mathbf{u}}{RT} \right)^2 - \frac{|\mathbf{u}|^2}{2RT} \right], \quad (37)$$

where W_α are the weight coefficients corresponding to particle discrete velocity $\boldsymbol{\xi}_\alpha$.

For the incompressible flow, the slight compressible effect will cause small numerical error in discrete Maxwellian distribution Eq. (37). To reduce this numerical error, the density can be approximately as $\rho = \rho_0 + \Delta\rho$ [40, 41]. Then, the following new type of equilibrium distribution function can be adopted in two-stage third-order DUGKS.

$$f_\alpha^{eq} = W_\alpha \left\{ \rho + \rho_0 \left[\frac{\xi_\alpha \cdot \mathbf{u}}{RT} + \frac{1}{2} \left(\frac{\xi_\alpha \cdot \mathbf{u}}{RT} \right)^2 - \frac{|\mathbf{u}|^2}{2RT} \right] \right\}. \quad (38)$$

Since only the nearly incompressible turbulent flows at constant temperature are considered in this paper, the following efficient D3Q19 model in Eq. (39) for discrete velocity space, which is originally used in the LBM method, can be adopted:

$$\begin{aligned} \xi &= \sqrt{3RT} \\ &\left[\begin{array}{cccccccccccccccccc} 0 & 1 & -1 & 0 & 0 & 0 & 1 & -1 & 1 & -1 & 1 & -1 & 1 & -1 & 1 & -1 & 0 & 0 & 0 \\ 0 & 0 & 0 & 1 & -1 & 0 & 0 & 1 & -1 & -1 & 1 & 0 & 0 & 0 & 0 & 1 & -1 & 1 & -1 \\ 0 & 0 & 0 & 0 & 0 & 1 & -1 & 0 & 0 & 0 & 0 & 1 & -1 & -1 & 1 & 1 & 1 & -1 & 1 \end{array} \right], \end{aligned} \quad (39)$$

where the associated weights are

$$W_\alpha = \begin{cases} 1/3 & \alpha = 0 \\ 1/18 & \alpha = 1, \dots, 6 \\ 1/36 & \alpha = 7, \dots, 18 \end{cases}. \quad (40)$$

2.3 Sub-grid scale model

Many SGS models have been proposed with the rapid development of LES method, most of them model the sub-grid scale tensor based on an eddy-viscosity assumption as follows:

$$\tau_{ij} - \frac{1}{3}\delta_{ij}\tau_{kk} = -2\nu_t \bar{S}_{ij}, \quad (41)$$

where ν_t is called SGS eddy viscosity, \bar{S}_{ij} is the symmetric part of the resolved velocity gradient. In the present high-order DUGKS, the effective viscosity can be expressed as the sum of molecular viscosity and eddy viscosity, therefore the effective relaxation time τ_e can be expressed as:

$$\tau_e = \frac{\nu_e}{RT} = \frac{\nu + \nu_t}{RT}. \quad (42)$$

The WALE model [16] and Vreman model [17] will be used to solve the near-wall region problem in present work, which offers a global coefficient SGS model that is affordable, easy to implement, and applicable to fully inhomogeneous flows. The turbulent eddy viscosity in the WALE model is calculated by the following

equations:

$$\begin{cases} \nu_t = (C_w \Delta)^2 \frac{(S_{ij}^d S_{ij}^d)^{3/2}}{(\bar{S}_{ij} \bar{S}_{ij})^{5/2} + (S_{ij}^d S_{ij}^d)^{5/4}}, \\ S_{ij}^d = \bar{S}_{ik} \bar{S}_{kj} + \bar{\Omega}_{ik} \bar{\Omega}_{kj} - \frac{1}{3} \delta_{ij} [\bar{S}_{mn} \bar{S}_{mn} - \bar{\Omega}_{mn} \bar{\Omega}_{mn}] . \end{cases} \quad (43)$$

with the model constant $C_w = 0.5 \sim 0.6$. The \bar{S}_{ij} and $\bar{\Omega}_{ij}$ are respective symmetric part and anti-symmetric part of the resolved velocity gradient:

$$\bar{S}_{ij} = \frac{1}{2} \left(\frac{\partial \bar{u}_i}{\partial x_j} + \frac{\partial \bar{u}_j}{\partial x_i} \right), \bar{\Omega}_{ij} = \frac{1}{2} \left(\frac{\partial \bar{u}_i}{\partial x_j} - \frac{\partial \bar{u}_j}{\partial x_i} \right). \quad (44)$$

In the Vreman model, the turbulent eddy viscosity is given by another template as follows:

$$\begin{cases} \nu_t = C_v \sqrt{B_\beta / (\alpha_{ij} \alpha_{ij})}, \\ \beta_{ij} = \Delta_m^2 \alpha_{mi} \alpha_{mj}, \\ B_\beta = \beta_{11} \beta_{22} + \beta_{11} \beta_{33} + \beta_{22} \beta_{22} - \beta_{12}^2 - \beta_{13}^2 - \beta_{23}^2. \end{cases} \quad (45)$$

where the symbol $\alpha_{ij} = \partial \bar{u}_i / \partial x_j$ represents the derivatives of the filtered velocity \bar{u} , B_β is an invariant of the matrix β_{ij} , while $\alpha_{ij} \alpha_{ij}$ is an invariant of $\alpha_{ij} \alpha_{ij}$. The model constant C_v is related to the Smagorinsky constant C_s by $C_v \approx 2.5 C_s^2$. In the present simulations, the WALE model employs model coefficient $C_w = 0.50$, and the Vreman model simulation employs $C_v = 0.07$. Moreover, the first-order derivatives of the velocity field in these models are calculated by a fourth-order central difference in the fully fluid cells, and the three-point scheme is used for the cells near wall boundary.

2.4 Computation procedure

In this section, the numerical procedure for one time step evolution of two-stage third-order DUGKS with force term is summarized as follows:

Step1: Compute the microscopic flux $L_j^{n+1/6}$ across the surface of control volumes from time t_n to $t_n + \Delta t/3$, and the half time step is set as $h = \Delta t/6$;

a) Solve the eddy viscosity ν_t at time t_n by WALE or Vreman model, and the effective relaxation time can be calculated by Eq. (42);

b) Solve the auxiliary distribution function $\bar{f}_j^{+,n}$ according to Eq. (46) and its spatial derivatives;

$$\bar{f}_j^{+,n} = f_j^n + \frac{h}{2} Q_j^n = f_j^n + \frac{\Delta t}{12} Q_j^n = \frac{12\tau - \Delta t}{12\tau + 3\Delta t} \hat{f}_j^n + \frac{4\Delta t}{12\tau + 3\Delta t} (1 + H\tau)_j^n f_j^{eq,n}. \quad (46)$$

c) Calculate the auxiliary distribution function $\bar{f}(\mathbf{x}_{cf}, \boldsymbol{\xi}, t_n + h)$ with Eq. (33) and Eq. (35), then calculate the density and velocity with Eq. (36);

d) Given the density and velocity, calculate the equilibrium distribution function $f^{eq}(\mathbf{x}_{cf}, \boldsymbol{\xi}, t_n + h)$ with Eq. (38);

- e) Calculate the original distribution function $f(\mathbf{x}_{cf}, \boldsymbol{\xi}, t_n + h)$ with Eq. (34);
- f) Calculate the microscopic flux $L_j^{n+1/6}$ with Eq. (14).

Step2: Compute the source term $Q_j^{n+1/3}$ as the sum of BGK collision operator and external force term;

- a) Calculate the auxiliary distribution function $\tilde{f}_j^{n+1/3}$ with Eq. (24), and $\tilde{f}_j^{+,n}$ can be solve with Eq. (27);
- b) Update the conservative flow variables $\mathbf{W}_j^{n+1/3}$ with Eq. (28), and update the equilibrium distribution function with Eq. (38);
- c) Solve the source term $Q_j^{n+1/3}$ with Eq. (29).

Step3: Compute the microscopic flux $L_j^{n+3/4}$ across the surface of control volumes from time $t_n + \Delta t/3$ to $t_n + 7\Delta t/6$, and the half time step is set as $h = 5\Delta t/12$;

- a) Solve the eddy viscosity v_t at time $t_n + \Delta t/3$ by WALE or Vreman model, and the effective relaxation time can be calculated by Eq. (42);
- b) Solve the auxiliary distribution function $\bar{f}_j^{+,n+1/3}$ according to Eq. (47) and its spatial derivatives;

$$\bar{f}_j^{+,n+1/3} = \frac{24\tau - 5\Delta t}{24\tau + 4\Delta t} \tilde{f}_j^{n+1/3} + \frac{9\Delta t}{24\tau + 4\Delta t} (1 + H\tau)_j^{n+1/3} f_j^{eq,n+1/3}. \quad (47)$$

- c) Calculate the auxiliary distribution function $\bar{f}(\mathbf{x}_{cf}, \boldsymbol{\xi}, t_n + \Delta t/3 + h)$ with Eq. (33) and Eq. (35), then calculate the density and velocity with Eq. (36);
- d) Given the density and velocity, calculate the equilibrium distribution function $f^{eq}(\mathbf{x}_{cf}, \boldsymbol{\xi}, t_n + \Delta t/3 + h)$ with Eq. (38);
- e) Calculate the original distribution function $f(\mathbf{x}_{cf}, \boldsymbol{\xi}, t_n + \Delta t/3 + h)$ with Eq. (34);
- f) Calculate the microscopic flux $L_j^{n+3/4}$ with Eq. (15).

Step4: Update distribution function with \hat{f}_j^{n+1} and conservative flow variables \mathbf{W}_j^{n+1} .

- a) Update auxiliary distribution function \hat{f}_j^{n+1} with Eq. (11);
- b) Update conservative flow variables \mathbf{W}_j^{n+1} .

3 Numerical results and discussions

3.1 The fully developed turbulent channel flow

The fully developed turbulent channel flow is a canonical wall-bounded turbulent flow, which has been simulated by many pioneers [1, 6, 44, 45] with macroscopic CFD methods. In addition, this case has also been simulated by several kinetic schemes based on mesoscopic models [11–13, 36]. The focus of this study is on validating the capability and accuracy of the present high-order DUGKS-based LES method for simulating the wall-bounded turbulent flows.

The parameter settings for the turbulent channel flow simulation are as follows. As shown in Fig. 1, the size of the non-dimensional domain is $(3\pi h, 2h, 4\pi h/3)$ in the streamwise (X coordinate), wall normal (Y coordinate) and spanwise (Z coordinate) directions, respectively. $Re_\tau = u_\tau h/\nu = 180$ with a kinematic viscosity of $\nu = 4.5 \times 10^{-5}$ is the Re number based on the friction velocity $u_\tau = \sqrt{\tau_w/\rho}$ and channel half-height h , where τ_w is the wall shear stress. In the simulation the channel half-height is set $h = 1$. Meanwhile, the characteristic viscous length scale

is defined as $\delta_h = \nu/u_\tau$, and the characteristic time scale is defined as $t_c = h/u_\tau$. The computational domain is divided into 1119744 cells ($108 \times 96 \times 108$ in X, Y and Z directions, respectively), where the uniform grids are used in streamwise and spanwise directions. In order to resolve the wall layer, a non-uniform mesh is used in the wall-normal direction, where the grid resolution is chosen as $\Delta y_{\min}^+ \approx 0.69$ and $\Delta y_{\max}^+ \approx 7.44$. Since the present high-order DUGKS is designed as a cell-centered finite volume scheme, the first recognizable point is located at a distance of $\Delta y^+ = 0.345$.

In the present simulations of turbulent channel flow, periodic boundaries are implemented in both the streamwise and spanwise directions, and the bounce-back treatment for distribution function [21] are applied at the solid walls to recover the macroscopic no-slip boundary condition. The initial density field is set to $\rho_0 = 1$, and the initial mean velocity is given by a laminar (Poiseuille) parabolic profile with divergence free perturbations satisfying wall boundary conditions. In addition, the uniform pressure gradient in the streamwise direction is implemented as a driving force, $F_x = -dp/dx = \rho_0 u_\tau^2/h$, and the forcing term will be adjusted at each time step [46] in order to obtain a constant mass-flux.

The simulation runs until stationary turbulence statistics are obtained. The initial run is carried out for approximately $55t_c$ to obtain a statistically stationary state. Then, an additional run is carried out for $24t_c$ to gather the average data. The averaging of flow quantities is performed in time as well as in space in the homogeneous directions (streamwise and spanwise directions).

Figure 2 shows the distribution of the streamwise mean velocity along the wall normal direction with wall-layer scaling laws, besides, the DNS result by Moser et al. [44] are plotted as well. It can be found in Fig. 2 that the present computed mean velocity profiles satisfy $u^+ = y^+$ in the viscous sublayer region ($y^+ \leq 5$) and logarithm law ($y^+ \geq 30$), i.e., $u^+ = A \ln y^+ + B$, where the values of $A = 2.5$ and $B = 5.5$ are known to be reasonably accurate for flow over smooth walls at $Re_\tau \approx 180$ [1, 3]. However, the present LES simulations over-predict the mean velocity profile in the log-law region by approximately 3.5%, and the results of the Vreman model and the WALE model almost coincide with each other. Such differences are likely due to the relatively coarser grids than DNS, in addition, they are also influenced by the numerical dissipation of the computational approach.

The profiles of root-mean-square (rms) velocity fluctuations are illustrated in Fig. 3(a), 3(b) and 3(c). The profiles from the Vreman and WALE models match well with each other, and they are both in reasonable agreement with the DNS results by Moser et al. [44]. In the buffer layer ($15 \leq y^+ \leq 60$), the present results in the streamwise and spanwise slightly deviate from the DNS data. Meanwhile, the rms velocity results in the normal direction show larger deviations than those in streamwise and spanwise. The Reynolds stress normalized by the wall-shear stress is presented in Fig. 3(d). The computed Reynolds stress profiles using Vreman and WALE models coincide with each other, and follow the DNS data [44] fairly closely with about 4% difference in the buffer regions. Similarly, due to the insufficient grid resolution, the present prediction of peak Reynolds stress is under the DNS data.

Figure 4 shows the computed rms pressure fluctuations, which are normalized by the wall shear stress and qualitatively consistent with the DNS results [44]. However,

there are also evident differences between the current results and the reference data. The computed maximum pressure fluctuations using different models have a maximum value of 1.75 at $y^+ \approx 34$, which is close to the DNS data, i.e., the value of 1.75 at $y^+ \approx 30$ [1] and 1.88 at $y^+ \approx 30$ [44], respectively. In addition, the present pressure fluctuation is about 1.46 at the wall boundary. It is smaller than prior data based DNS in Ref [1, 44] whose values are about 1.50 and 1.53, respectively. As discussed in Ref [11, 12], such difference could conceivably be due to compressibility effects and filter effects.

Further comparisons about the fluctuations of rms vorticity components are illustrated in Fig. 5. Being same with the above analysis, the results of Vreman model and WALE model are almost the same, and all of them are qualitatively consistent with the reference data [44]. Because of the inhomogeneity and anisotropy of turbulence closer to the wall, it is found that there are evident differences among the components of vorticity. In addition, as expected, all the components of vorticity away from the wall tend to be consistent value.

3.2 The turbulent plane Couette flow

Most of the research has been carried out in the fully developed turbulent channel flow, while the study of turbulent plane Couette flow [47, 48] was relatively few. One of the reasons is the existence of very-large-scale motions in Couette flow [48, 49] (especially for large Re number) that is particularly challenging to implement DNS, and therefore LES may be a good alternative [48].

In this sub-section, a turbulent plane Couette flow at low friction Re number ($Re_\tau = 93$) will be investigated. The flow domain ($4\pi h$ in the streamwise, $2h$ in the wall normal and $2\pi h$ in the spanwise directions) and coordinate system are shown in Fig. 6. In the simulation the half distance between the walls is set $h = 1$. Meanwhile, the characteristic viscous length scale is defined as $\delta_h = \nu/u_\tau$, and the characteristic time scale is defined as $t_c = h/u_\tau$, where the $\nu = 4.95 \times 10^{-5}$ is kinematic viscosity and u_τ is the friction velocity. The computational domain is divided into $(108 \times 96 \times 108)$ in the streamwise (X coordinate), wall normal (Y coordinate) and spanwise (Z coordinate) directions, respectively, where the uniform grids are used in streamwise and spanwise directions. In order to resolve the wall layer, a non-uniform mesh is used in the wall-normal direction, where the grid resolution is chosen as $\Delta y_{\min}^+ \approx 0.44$ and $\Delta y_{\max}^+ \approx 3.59$.

In the present simulations, the initial density field is set to $\rho_0 = 1$, and the initial velocity is given by a laminar (Couette) linear profile with divergence free perturbations satisfying wall boundary conditions. The statistical average of flow quantities is performed in time about $36t_c$ as well as in space in the homogeneous directions until stationary are obtained.

The computed streamwise mean velocity profiles along the wall normal direction are shown in Fig. 7 scaled in outer (Fig. 7(a)) and inner (Fig. 7(b)) units. In Fig. 7(b) the $u^+ = y^+$ in the viscous sublayer region ($y^+ \leq 5$) and logarithm law $u^+ = \ln y^+/\kappa + B$ in the near-wall log-law region ($y^+ \geq 30$) have been plotted for $\kappa = 0.41$ and $B = 5.1$. The present profiles of both the Vreman and WALE models agree well with the DNS results of Lee and Moser [48], where the maximum deviation from DNS data in log-law region is approximately 2.3% for Vreman model and 2.0% for WALE model.

The rms velocity fluctuations are illustrated in Fig. 8(a), 8(b) and 8(c). The rms velocity profiles from the Vreman and WALE models match well with each other, and they are both in reasonable agreement with the DNS results by Lee and Moser [48]. In the region of $15 \leq y^+ \leq 50$, the v'_{rms} and w'_{rms} slightly deviate from the DNS data, while u'_{rms} deviates from the DNS data in the region of $y^+ \geq 40$. The Reynolds stress is also presented in Fig. 8(d). Different from the turbulent channel flow, in plane Couette flow, the Reynolds stress increases monotonically from the wall to an almost constant level in the centre region. It can be found that the present computed Reynolds stress profiles by Vreman and WALE models obviously deviate from that computed by direct numerical simulations [48] in the region of $y^+ \geq 20$, especially for the result of WALE model near the buffer layer. These deviations may be due to the follow reasons. Firstly, the grids in the streamwise and spanwise directions are relatively coarser than wall normal direction. Secondly, owing to great computational cost, the computational domain size (the streamwise and spanwise directions) for the present work is not long enough to cover the extent of the large-scale motion in Couette flow [47, 48]. It should be noted that the selected computational domain is sufficient for the present research purpose, and capturing and studying all the very-large-scale motions is out of scope for the current study.

The computed rms pressure fluctuations normalized by the wall shear stress are illustrated in Fig. 9, which are reasonably consistent with the DNS results [48]. The rms pressure fluctuation at the wall boundary is about 2.41 for Vreman model and 2.44 for WALE model, which are close to the prior data based DNS in Ref [48] whose value is about 2.37. Figure 10 shows the rms of vorticity fluctuations components. Being same with the turbulent channel flow, the results of Vreman model and WALE model are almost the same, and all of them are qualitatively consistent with the DNS results [48].

3.3 Three-dimensional lid-driven cubical cavity flow

The two-dimensional lid-driven cavity flow is a classic benchmark case for testing new numerical methods or studying additional physical effects of flow phenomenon [50]. The three-dimensional cavity flow has also attracted vast amount of attention and has been studied both experimentally [51] and numerically [11, 52–54]. This section focuses on relatively high Reynolds-number ($Re = 12000$) lid-driven cubical cavity flows. Generally speaking, when the Reynolds number based on the lid-driven velocity and cavity length is less than 2000, the flow is laminar. At Reynolds number higher than the critical value between 2000 and 3000, an instability appears in the vicinity of the downstream-corner-eddy [55]. Although the critical Reynolds number is not clear, with the further increase of Re , there is turbulence over some part of the flow field. At Reynolds number higher than 10000, the flow near the downstream-corner-eddy becomes fully turbulent.

The three-dimensional lid-driven cubical cavity flow has a simple geometry, while it contains complex flow phenomena [52]. In addition, there is not any homogeneous flow direction, and the presence of side walls affects the full flow patterns. Due to the complex flow phenomena encountered within such a system at higher Re , it becomes a very challenging case. Especially, it requires accurate time and space discretization methods to obtain results with long averaging times. Consequently, the present

LES-based high-order DUGKS method will be used to study this problem, and its numerical capability is testified.

The fluid enclosed in the cavity is assumed to be nearly incompressible, Newtonian with uniform density and temperature. The flow domain of the lid-driven cubical cavity of length $2L$ is shown in Fig. 11(a) with coordinate system, in which flow is driven by the top lid that moves in the x -direction with maximum velocity $U_w = 0.15$ to keep the $Ma = U_w/\sqrt{3RT} \ll 1$. Consequently, the Reynolds number used in our computations is $Re = (2LU_w)/\nu = 12000$ with a viscosity of $\nu = 2.5 \times 10^{-5}$. In order to obtain an efficient near-wall resolution, the stretching smooth grid of $64 \times 64 \times 64$ in Fig. 11(b) is adopted (refined grid is used near wall boundary).

In the present simulations, the time step is chosen as 8.4×10^{-4} , and a statistically stationary state of the flow field is achieved after running for $510t_c$. In addition, the computed turbulence statistics, including mean velocity, Reynolds stress profiles, and rms velocity fluctuations were obtained by a long time averaging about $600t_c$, where the characteristic time is $t_c = 2L/U_w$.

As far as the constant velocity is imposed on the lid, it will lead to severe discontinuities along the top edges. Moreover, the presence of such discontinuities may undermine the accuracy and stability of numerical simulations [52, 53]. In order to remove these weakness, A high degree polynomial velocity distribution as Eq. (48) on the lid is adopted according to the recommendation of Leriche and Gavrilakis [52].

$$u_w(x, 2L, z) = U_w \left[1 - \left(\frac{x}{L} - 1 \right)^{18} \right]^2 \times \left[1 - \left(\frac{z}{L} - 1 \right)^{18} \right]^2, \quad (48)$$

where the moving boundary is at $y = 2L$ (top wall) and U_w is the maximum velocity. This profile in Eq. (48) makes the velocity zero value at the intersection between the top wall and other walls, meanwhile, the lid-driven velocity grows rapidly to a constant value over a short distance away from side walls.

The mean velocity profiles along the horizontal (x -direction) and vertical (y -direction) symmetry axes are shown in Fig. 12. The predictions by both WALE and Vreman models are found to be in good agreement with DNS data of Leriche and Gavrilakis [52] and LES predictions by Shetty et al. [54] with dynamic Vreman model, except that $x - < v >$ profile (Fig. 12(a), mean velocity $< v >$ along x direction) is smaller than DNS data at the negative peak. As discussed in Ref. [52], the narrow peak near the downstream wall indicates that the flow in these regions is laminar but unsteady. It is also obvious from the velocity profiles that the flow parallel to the downstream wall is similar to a wall jet, rather than a boundary layer. As shown in Fig. 12(b), it also contains a high average velocity gradient in the thin high momentum layer near the lid. The kinetic energy is injected into the flow by the shear stress at the top lid. The present prediction of the distance that the mean velocity $< u >$ falling by half along the normal direction at the center of the lid is about 0.87% (0.874% for Vreman model and 0.872% for WALE model) of the separation between the cavity walls, which is in agreement with 0.8% of Leriche and Gavrilakis [52].

The contour plots of the mean velocity component $< u >$ and $< v >$ in the mid-plane $Z = 1$ are shown in Fig. 13. The present results correctly capture all

secondary corner eddies next to the upstream wall and located near the upper wall or bottom wall in the mean flow field. Furthermore, there is almost no difference between the two SGS models in prediction of the mean flow structure. The most dominant features of the mean flow is the large-scale recirculation which spans the cavity [52]. As shown in Fig. 14, the flow in the thin high-momentum layer next to the lid changes its direction around the upper corner near the downstream. Then, the flow develops into an unsteady wall jet whose thickness varies along the downstream wall, and breaks up into two approximately elliptical free jets (also see Fig. 15). The prediction of the plane wall jet separates from the downstream wall at distances Δy (from the bottom wall) of about $0.5L - 0.6L$, which is in line with the DNS data of Leriche and Gavrilakis [52]. As shown in Fig. 15, the flow pattern is that: the flow structures (especially the wall jets) on both sides of the symmetry plane ($Z = 1$) are similar.

The profiles of rms velocity fluctuations along two lines $(x, 1, 1)$ and $(1, y, 1)$ are shown in Fig. 16. The present results show that the rms fluctuations along the line $(x, 1, 1)$ (Fig. 16(a) and Fig. 16(b)) are in good agreement with the DNS [52], except for the slight deviations at the peak. For results along the line $(1, y, 1)$ (Fig. 16(c) and Fig. 16(d)), there are obvious deviations near the peaks of the fluctuations when compared with the DNS data. Considering that the DNS solution was obtained by a Chebyshev collocation method on a grid composed of 129 collocation points in each spatial direction ,while the present method with LES model uses only 65-points in each direction, the present results are acceptable and in reasonable agreement with the DNS [52]. As for the comparison with LES data [54] provided by fifth-order WENO scheme and dynamic Vreman model under the same grid, the present results are good. In addition, the predictions made by Vreman model and WALE model have slight differences. The components of the Reynolds stress $\langle u'v' \rangle$ on these two central lines are also provided in Fig. 17. The differences between the profiles predicted by the present two LES models are inconspicuous. They both consistent to the trend of the DNS data, while their maximums tend to be slightly underestimated by LES, whereas their minimums are somewhat overestimated.

The present results explicitly indicate that turbulence is generated on cavity walls. It is obvious that the turbulent fluctuations are about one order of magnitude larger near the downstream wall than near the upstream wall. Moreover, the fluctuations on the bottom wall are the largest. In the region near the downstream wall where the wall jet separated into two elliptical jets, the high gradients of velocity fluctuations are also well reproduced. In addition, the Reynolds stress below the top lid is small that can be ignored, which indeed shows that the flow under the lid is mainly laminar but transient. These physics seem to be consistent with the descriptions in the abundant literature which studying this problem [52, 53]. The present high-order DUGKS-based LES method can simulate inhomogeneous wall-bounded turbulent flows and get reliable results.

4 Summary

In present work, both the incompressible discrete Maxwellian equilibrium distribution function and the external force were introduced into the two-stage third-order DUGKS for simulating low-speed incompressible turbulent flow. In addition, a parallel code with three-dimensional domain decomposition based on the two-stage

third-order DUGKS with forcing term for large-eddy simulation of turbulent flows was developed. Three typical wall-bounded turbulent flows, the fully developed turbulent channel flow at $Re_\tau \approx 180$, the turbulent plane Couette flow with a friction Reynolds number $Re_\tau \approx 93$ and lid-driven cubical cavity flow at $Re = 12000$ were investigated using the present high-order DUGKS method (based on D3Q19 model) with the aid of the Vreman and the WALE sub-grid models.

The turbulence statistics, including mean velocity, the rms fluctuations velocity, Reynolds stress, the rms fluctuations pressure and vorticity are compared with the benchmark DNS data given in the previous literatures. It was no surprise that the results from the Vreman and WALE models are in perfect agreement with each other, and they are both in reasonable agreement with the DNS data. However, for the fully developed turbulent channel flow, there were some deviations in comparison with the DNS results, especially for the rms vorticity fluctuations and the rms pressure fluctuation, which may be caused by the relatively coarse grid and filter effects. As for lid-driven cubical cavity flow, the predictions of mean velocity field using WALE and Vreman models are in good agreement with the DNS data. Although the results of the rms fluctuations of velocity field and Reynolds stress slightly deviate from the DNS data, the flow physics are consistent with the descriptions of the abundant literature.

In summary, the LES for wall-bounded turbulent flows using high-order DUGKS shows that its results (with a relatively coarse grid) are reasonably accurate when compared to the DNS. It clearly proves that the present high-order DUGKS has the potential to be used as a LES tool for simulating turbulent flows. However, we should also note that the flow Reynolds number of the current examples are not too high, large-eddy simulations of turbulent flow at extremely high flow Reynolds numbers are needed to further verify the capabilities and accuracy of the present method in the recent future.

Acknowledgments

The authors thank National Supercomputing Center in Wuxi and Shanghai Supercomputing Technology Co., LTD for providing computing resources.

Authors' contributions

All authors read and approved the final manuscript.

Funding

The National Numerical Wind Tunnel Project, the National Natural Science Foundation of China (Grant No. 11902264, 11902266), and the 111 Project of China (B17037).

Availability of data and materials

The data that support the findings of this study are available from the corresponding author upon reasonable request.

Competing interests

The authors declare that they have no competing interests.

Author details

¹School of Aeronautics, Northwestern Polytechnical University, 127 West Youyi Road, 710072, Xi'an, P.R.China.

²National Key Laboratory of Science and Technology on Aerodynamic Design and Research, Northwestern Polytechnical University, 127 West Youyi Road, 710072, Xi'an, P.R.China.

References

1. Kim, J., Moin, P., Moser, R.: Turbulence statistics in fully developed channel flow at low Reynolds number. *Journal of Fluid Mechanics* **177**, 133–166 (1987)
2. Moin, P., Mahesh, K.: Direct numerical simulation: A tool in turbulence research. *Annual Review of Fluid Mechanics* **30**, 539–578 (1998)
3. Pope, S.B.: *Turbulent Flows*. Cambridge University Press, New York (2000)

4. Wilcox, D.C.: Turbulence Modeling for CFD. DCW Industries, Inc., La Canada, California (2006)
5. Smagorinsky, J.: General circulation experiments with the primitive equations: I. The basic experiment. *Monthly Weather Review* **91**(3), 99–164 (1963)
6. Deardorff, J.W.: A numerical study of three-dimensional turbulent channel flow at large Reynolds numbers. *Journal of Fluid Mechanics* **41**(2), 453–480 (1970)
7. Meneveau, C., Katz, J.: Scale-invariance and turbulence models for large-eddy simulation. *Annual Review of Fluid Mechanics* **32**, 1–32 (2000)
8. Sagaut, P.: Large Eddy Simulation for Incompressible Flows: An Introduction. Springer, Berlin (2006)
9. Bose, S.T., Park, G.I.: Wall-modeled large-eddy simulation for complex turbulent flows. *Annual Review of Fluid Mechanics* **50**, 535–561 (2018)
10. Chen, H., Kandasamy, S., Orszag, S., Shock, R., Succi, S., Yakhot, V.: Extended Boltzmann kinetic equation for turbulent flows. *Science* **301**(5633), 633–636 (2003)
11. Premnath, K.N., Pattison, M.J., Banerjee, S.: Generalized lattice Boltzmann equation with forcing term for computation of wall-bounded turbulent flows. *Physical Review E* **79**(2), 026703 (2009)
12. Liu, M., Chen, X., Premnath, K.N.: Comparative study of the large eddy simulations with the lattice Boltzmann method using the wall-adapting local eddy viscosity and Vreman subgrid scale models. *Chinese Physics Letters* **29**(10), 104706 (2012)
13. Zhuo, C., Zhong, C.: LES-based filter-matrix lattice Boltzmann model for simulating fully developed turbulent channel flow. *International Journal of Computational Fluid Dynamics* **30**(7-10), 543–553 (2016)
14. S., H., J., S., S., C., GD, D.: A lattice boltzmann subgrid model for high Reynolds number flows. *Fields Institute Communications* **6**(13), 151–166 (1996)
15. Premnath, K.N., Pattison, M.J., Banerjee, S.: Dynamic subgrid scale modeling of turbulent flows using lattice-Boltzmann method. *Physica A-Statistical Mechanics and its Applications* **388**(13), 2640–2658 (2009)
16. Nicoud, F., Ducros, F.: Subgrid-scale stress modelling based on the square of the velocity gradient tensor. *Flow, Turbulence and Combustion* **62**(3), 183–200 (1999)
17. Vreman, A.W.: An eddy-viscosity subgrid-scale model for turbulent shear flow: Algebraic theory and applications. *Physics of Fluids* **16**(10), 3670–3681 (2004)
18. Xu, K.: A gas-kinetic BGK scheme for the NavierStokes equations and its connection with artificial dissipation and Godunov method. *Journal of Computational Physics* **171**(1), 289–335 (2001)
19. Su, M., Yu, J.D.: A parallel large eddy simulation with unstructured meshes applied to turbulent flow around car side mirror. *Computers & Fluids* **55**, 24–28 (2012)
20. Cao, G., Su, H., Xu, J., Xu, K.: Implicit high-order gas kinetic scheme for turbulence simulation. *Aerospace Science and Technology* **92**, 958–971 (2019)
21. Guo, Z., Xu, K., Wang, R.: Discrete unified gas kinetic scheme for all Knudsen number flows: Low-speed isothermal case. *Physical Review E* **88**(3), 033305 (2013)
22. Guo, Z., Wang, R., Xu, K.: Discrete unified gas kinetic scheme for all Knudsen number flows. II. Thermal compressible case. *Physical Review E* **91**(3), 033313 (2015)
23. Xu, K., Huang, J.-C.: A unified gas-kinetic scheme for continuum and rarefied flows. *Journal of Computational Physics* **229**(20), 7747–7764 (2010)
24. Zhu, L., Guo, Z., Xu, K.: Discrete unified gas kinetic scheme on unstructured meshes. *Computers & Fluids* **127**, 211–225 (2016)
25. Wu, C., Shi, B., Chai, Z., Wang, P.: Discrete unified gas kinetic scheme with a force term for incompressible fluid flows. *Computers & Mathematics with Applications* **71**(12), 2608–2629 (2016)
26. Pan, D., Zhong, C., Zhuo, C.: An implicit discrete unified gas-kinetic scheme for simulations of steady flow in all flow regimes. *Communications in Computational Physics* **25**(5), 1469–1495 (2019)
27. Zhu, Y., Zhong, C., Xu, K.: Implicit unified gas-kinetic scheme for steady state solutions in all flow regimes. *Journal of Computational Physics* **315**, 16–38 (2016)
28. Liu, H., Kong, M., Chen, Q., Zheng, L., Cao, Y.: Coupled discrete unified gas kinetic scheme for the thermal compressible flows in all Knudsen number regimes. *Physical Review E* **98**(5), 053310 (2018)
29. Chen, J., Liu, S., Wang, Y., Zhong, C.: Conserved discrete unified gas-kinetic scheme with unstructured discrete velocity space. *Physical Review E* **100**(4), 043305 (2019)
30. Zhang, C., Yang, K., Guo, Z.: A discrete unified gas-kinetic scheme for immiscible two-phase flows. *International Journal of Heat and Mass Transfer* **126**, 1326–1336 (2018)
31. Yang, Z., Zhong, C., Zhuo, C.: Phase-field method based on discrete unified gas-kinetic scheme for large-density-ratio two-phase flows. *Physical Review E* **99**(4), 043302 (2019)
32. Zhang, Y., Zhu, L., Wang, R., Guo, Z.: Discrete unified gas kinetic scheme for all Knudsen number flows. III. Binary gas mixtures of Maxwell molecules. *Physical Review E* **97**(5), 053306 (2018)
33. Tao, S., Zhang, H., Guo, Z., Wang, L.: A combined immersed boundary and discrete unified gas kinetic scheme for particlefluid flows. *Journal of Computational Physics* **375**, 498–518 (2018)
34. Song, X., Zhang, C., Zhou, X., Guo, Z.: Discrete unified gas kinetic scheme for multiscale anisotropic radiative heat transfer. *Advances in Aerodynamics* **2**(3), 1–15 (2020)
35. Wang, P., Wang, L., Guo, Z.: Comparison of the lattice Boltzmann equation and discrete unified gas-kinetic scheme methods for direct numerical simulation of decaying turbulent flows. *Physical Review E* **94**(4), 043304 (2016)
36. Bo, Y., Wang, P., Guo, Z., Wang, L.: DUGKS simulations of three-dimensional TaylorGreen vortex flow and turbulent channel flow. *Computers & Fluids* **155**, 9–21 (2017)
37. Wu, C., Shi, B., Shu, C., Chen, Z.: Third-order discrete unified gas kinetic scheme for continuum and rarefied flows: Low-speed isothermal case. *Physical Review E* **97**(2), 023306 (2018)
38. Li, J., Du, Z.: A two-stage fourth order time-accurate discretization for Lax-Wendroff type flow solvers I. Hyperbolic conservation laws. *SIAM Journal on Scientific Computing* **38**(5), 3046–3069 (2016)
39. Li, J.: Two-stage fourth order: temporal-spatial coupling in computational fluid dynamics (CFD). *Advances in Aerodynamics* **1**(3), 1–36 (2019)

40. Zou, Q., Hou, S., Chen, S., Doolen, G.D.: An improved incompressible lattice Boltzmann model for time-independent flows. *Journal of Statistical Physics* **81**(1-2), 35–48 (1995)
41. He, X., Luo, L.: Lattice Boltzmann model for the incompressible NavierStokes equation. *Journal of Statistical Physics* **88**(3/4), 927–944 (1997)
42. Bhatnagar, P.L., Gross, E.P., Krook, M.: A model for collision processes in gases. i. small amplitude processes in charged and neutral one-component systems. *Physical Review* **94**, 511–525 (1954)
43. He, X., Chen, S., Doolen, G.D.: A novel thermal model for the lattice Boltzmann method in incompressible limit. *Journal of Computational Physics* **146**(1), 282–300 (1998)
44. Moser, R.D., Kim, J., Mansour, N.N.: Direct numerical simulation of turbulent channel flow up to $Re_\tau=590$. *Physics of Fluids* **11**(4), 943–945 (1999)
45. Vreman, A.W., Kuerten, J.G.M.: Comparison of direct numerical simulation databases of turbulent channel flow at $Re_\tau = 180$. *Physics of Fluids* **26**(1), 015102 (2014)
46. Gokarn, A., Battaglia, F., Fox, R.O., Hill, J.C., Reveillon, J.: Large eddy simulations of incompressible turbulent flows using parallel computing techniques. *International Journal for Numerical Methods in Fluids* **56**(10), 1819–1843 (2008)
47. Bech, K.H., Tillmark, N., Alfredsson, P.H., Andersson, H.I.: An investigation of turbulent plane Couette flow at low Reynolds numbers. *Journal of Fluid Mechanics* **286**, 291–325 (1995)
48. Lee, M., Moser, R.D.: Extreme-scale motions in turbulent plane Couette flows. *Journal of Fluid Mechanics* **842**, 128–145 (2018)
49. Tsukahara, T., Kawamura, H., Shingai, K.: DNS of turbulent Couette flow with emphasis on the large-scale structure in the core region. *Journal of Turbulence* **7**(19), 1–16 (2006)
50. Ghia, U., Ghia, K.N., Shin, C.T.: High-Re solutions for incompressible flow using the Navier-Stokes equations and a multigrid method. *Journal of Computational Physics* **48**(3), 387–411 (1982)
51. Prasad, A.K., Koseff, J.R.: Reynolds number and endwall effects on a liddriven cavity flow. *Physics of Fluids A: Fluid Dynamics* **1**(2), 208–218 (1989)
52. Leriche, E., Gavrilakis, S.: Direct numerical simulation of the flow in a lid-driven cubical cavity. *Physics of Fluids* **12**(6), 1363–1376 (2000)
53. Bouffanais, R., Deville, M.O., Leriche, E.: Large-eddy simulation of the flow in a lid-driven cubical cavity. *Physics of Fluids* **19**(5), 055108 (2007)
54. Shetty, D.A., Fisher, T.C., Chunekar, A.R., Frankel, S.H.: High-order incompressible large-eddy simulation of fully inhomogeneous turbulent flows. *Journal of Computational Physics* **229**(23), 8802–8822 (2010)
55. Iwatsu, R., Ishii, K., Kawamura, T., Kuwahara, K., Hyun, J.M.: Numerical simulation of three-dimensional flow structure in a driven cavity. *Fluid Dynamics Research* **5**(3), 173–189 (1989)

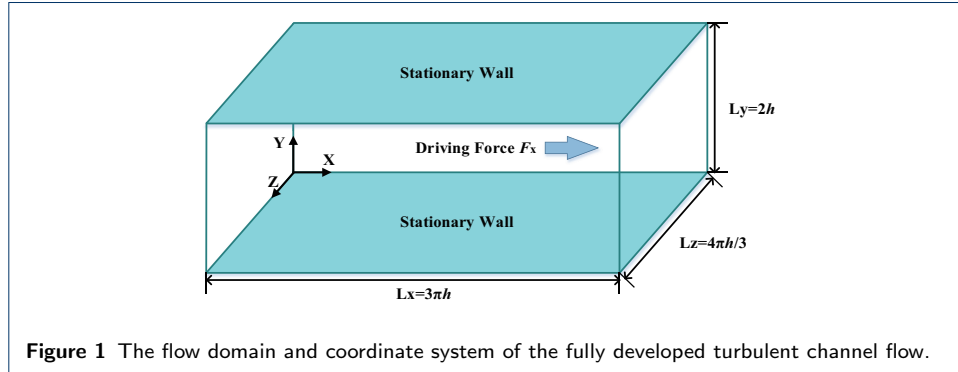
Figures

Figure 1 The flow domain and coordinate system of the fully developed turbulent channel flow.

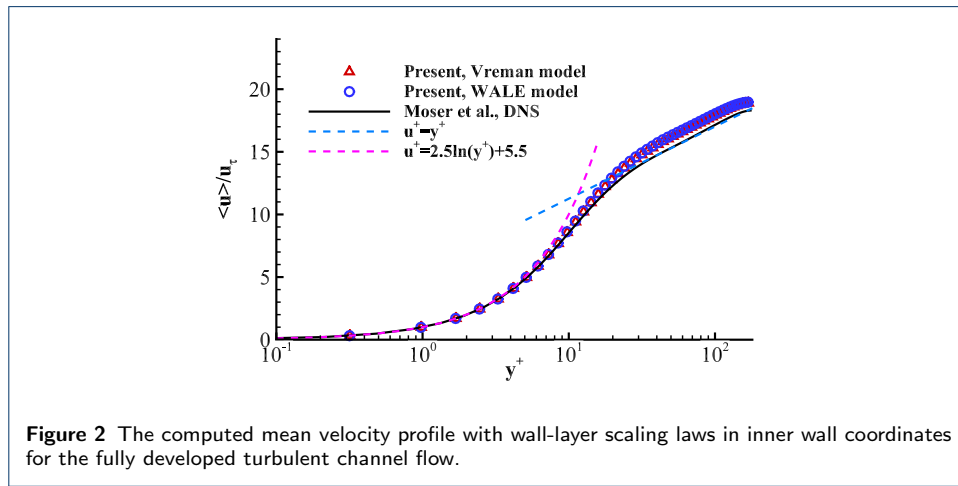
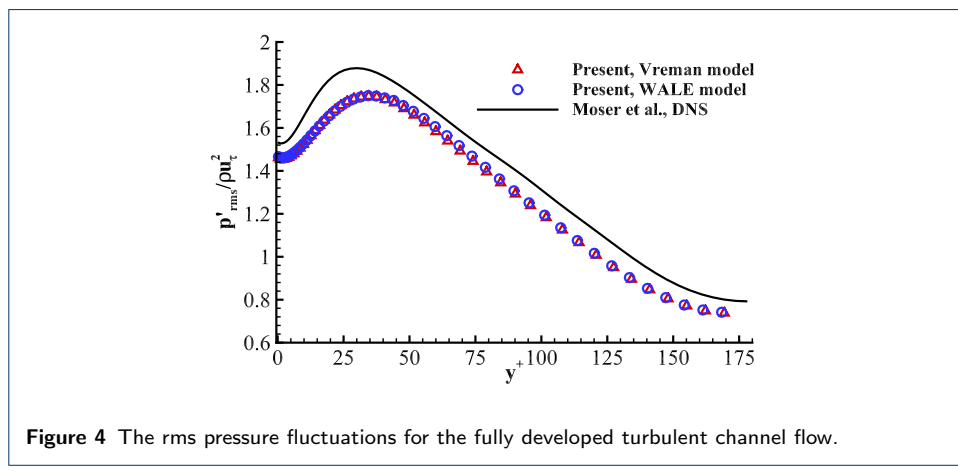
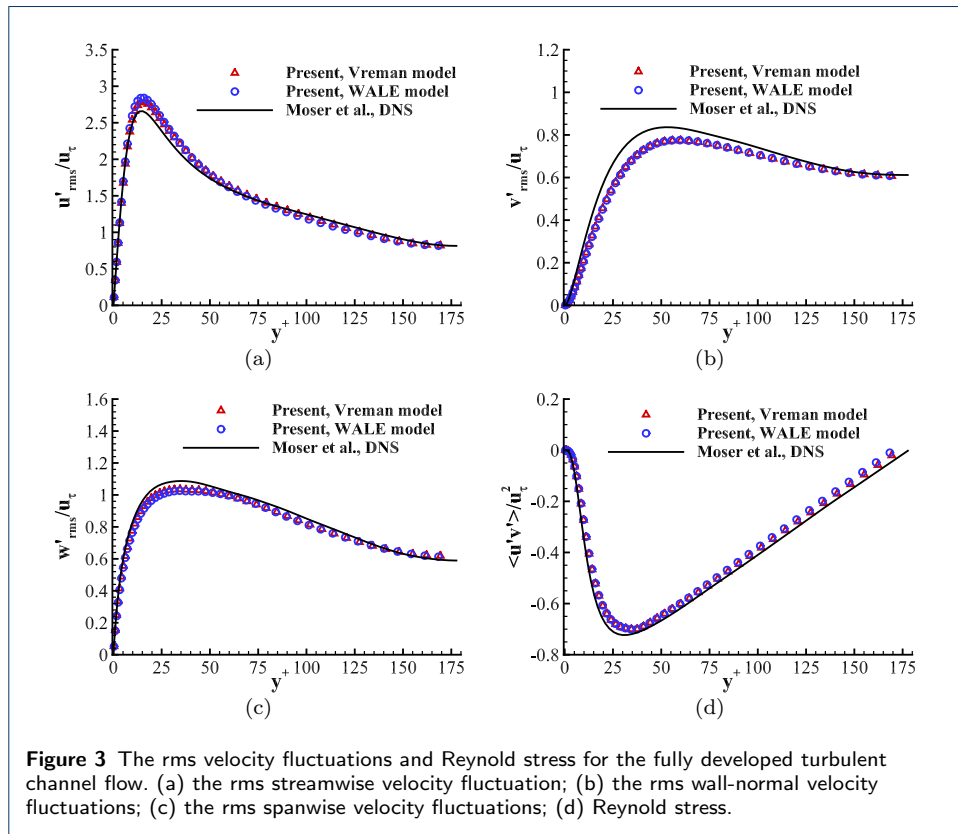


Figure 2 The computed mean velocity profile with wall-layer scaling laws in inner wall coordinates for the fully developed turbulent channel flow.



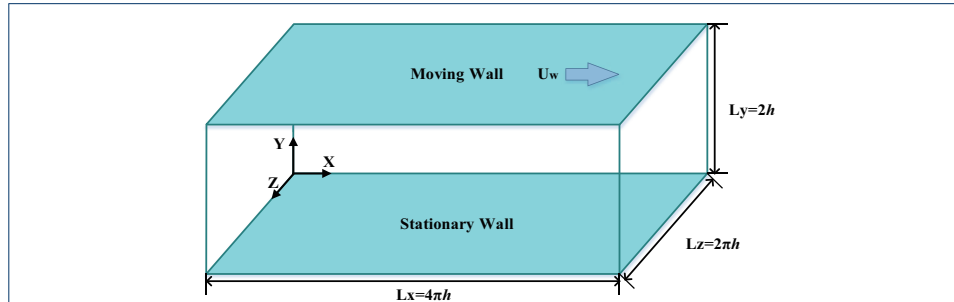
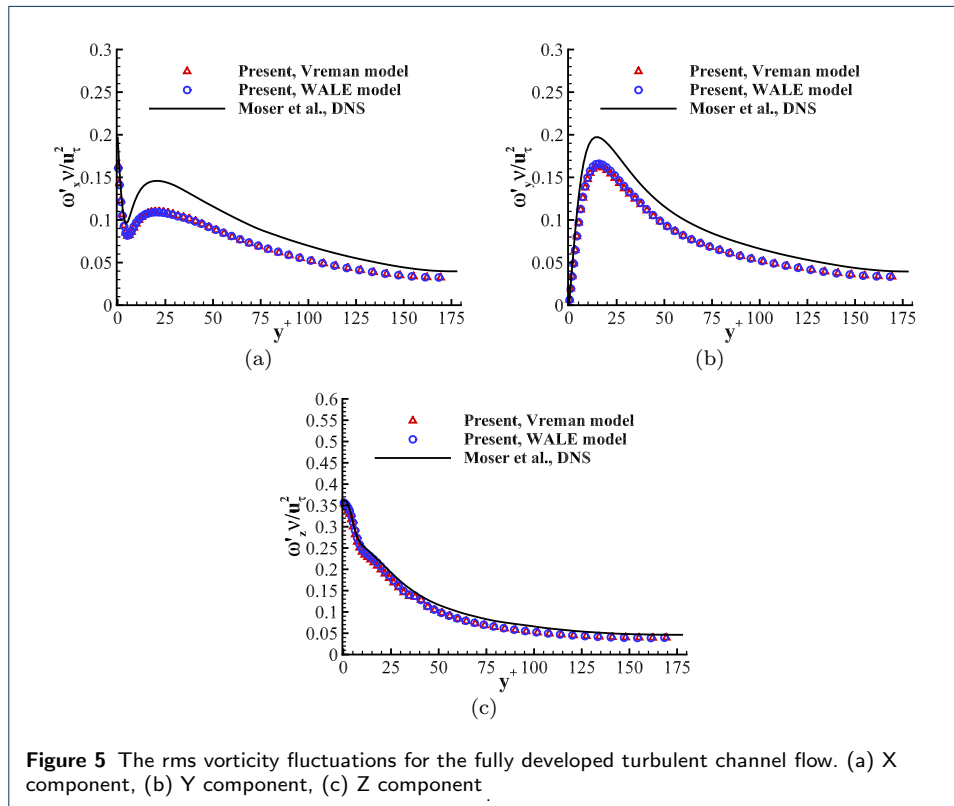
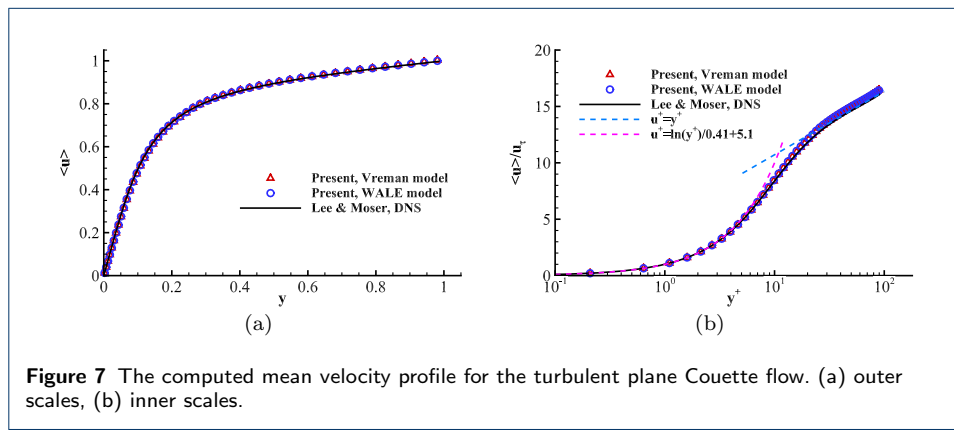
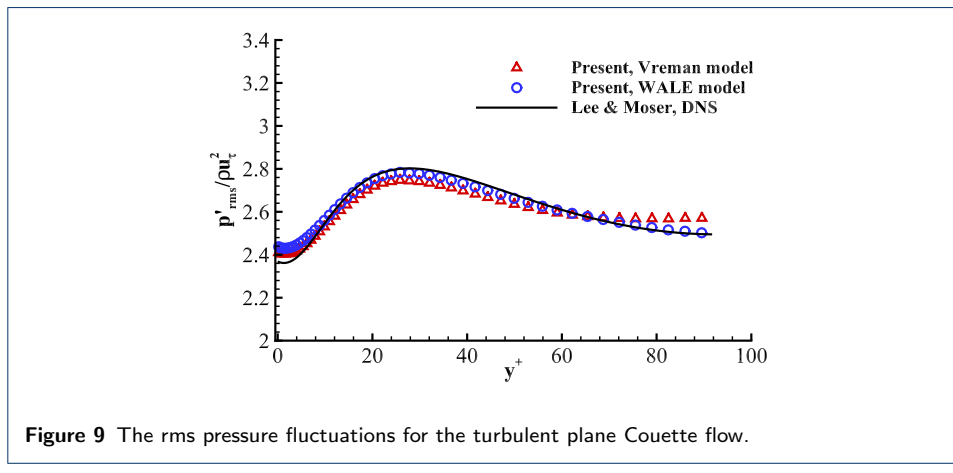
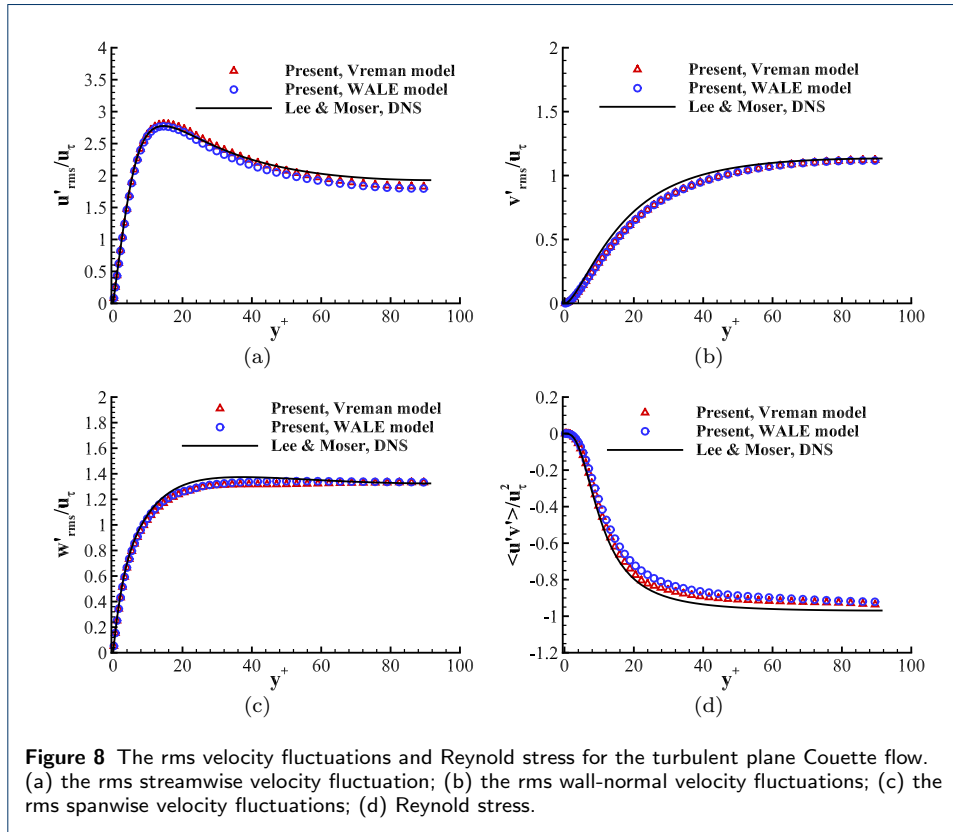
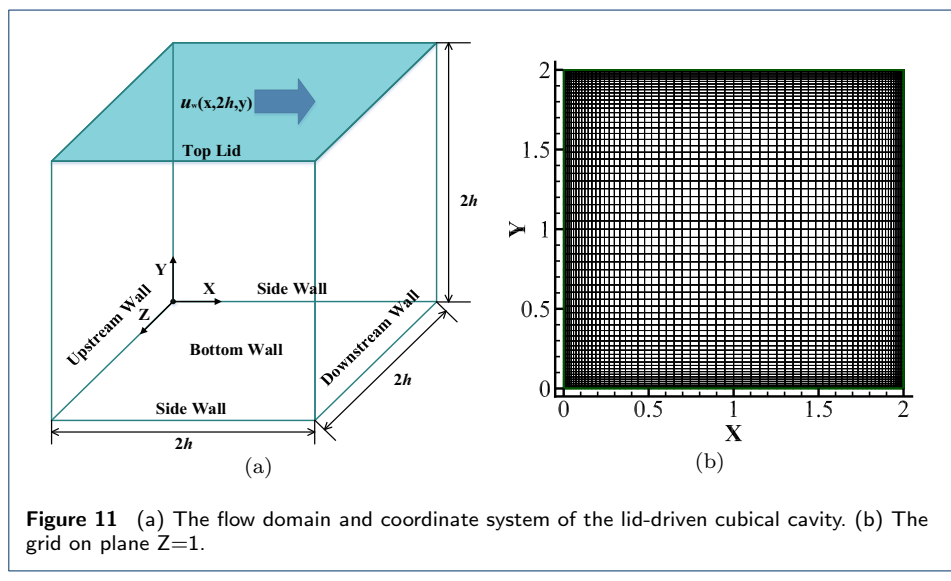
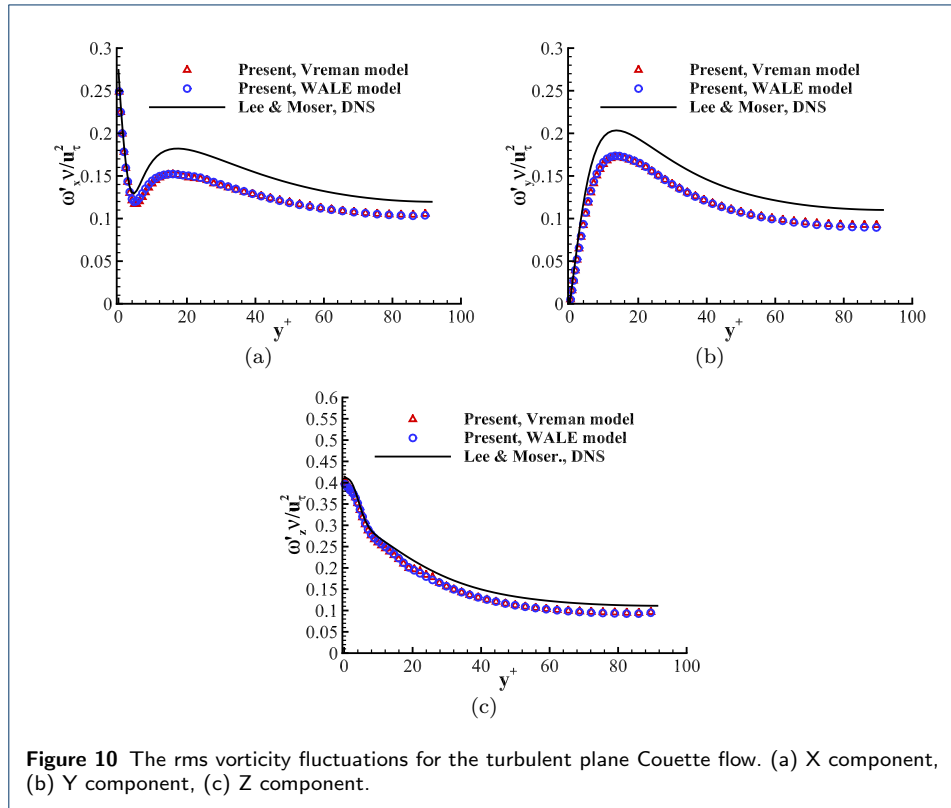


Figure 6 The flow domain and coordinate system of the turbulent plane Couette flow.







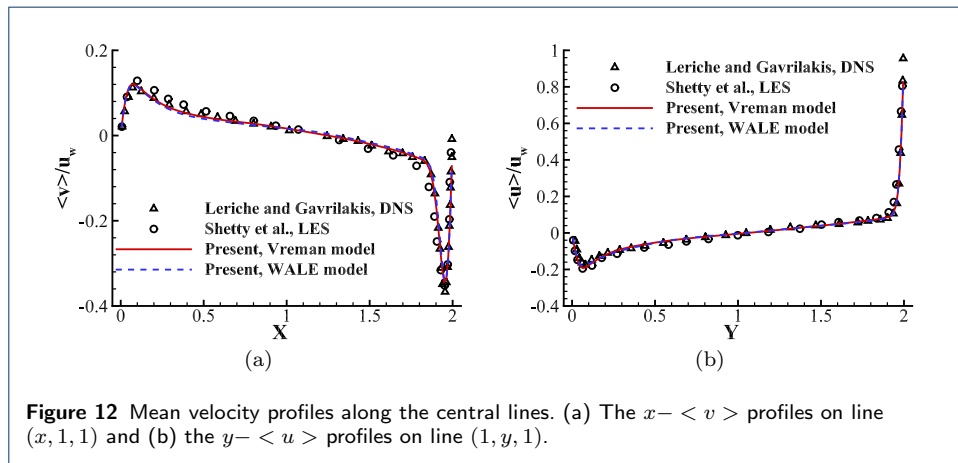


Figure 12 Mean velocity profiles along the central lines. (a) The $x - \langle v \rangle$ profiles on line $(x, 1, 1)$ and (b) the $y - \langle u \rangle$ profiles on line $(1, y, 1)$.

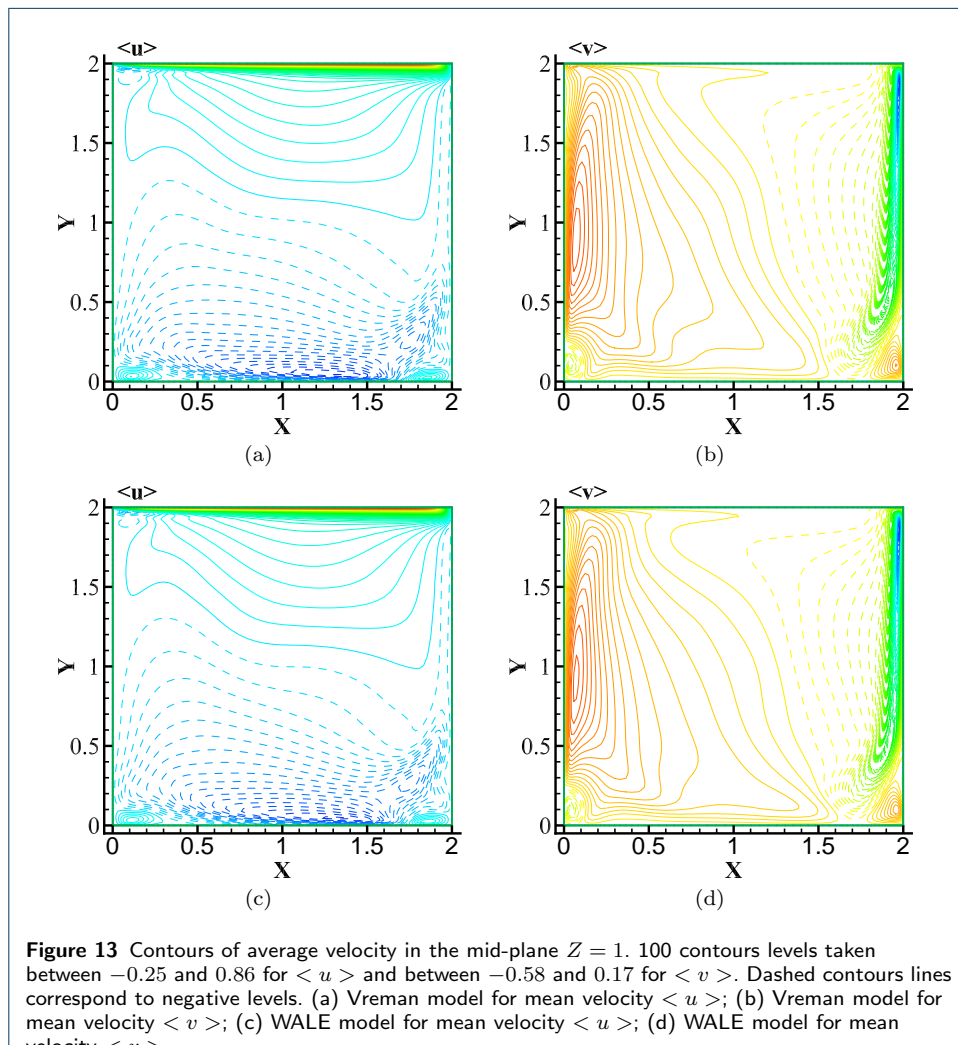


Figure 13 Contours of average velocity in the mid-plane $Z = 1$. 100 contours levels taken between -0.25 and 0.86 for $\langle u \rangle$ and between -0.58 and 0.17 for $\langle v \rangle$. Dashed contours lines correspond to negative levels. (a) Vreman model for mean velocity $\langle u \rangle$; (b) Vreman model for mean velocity $\langle v \rangle$; (c) WALE model for mean velocity $\langle u \rangle$; (d) WALE model for mean velocity $\langle v \rangle$.

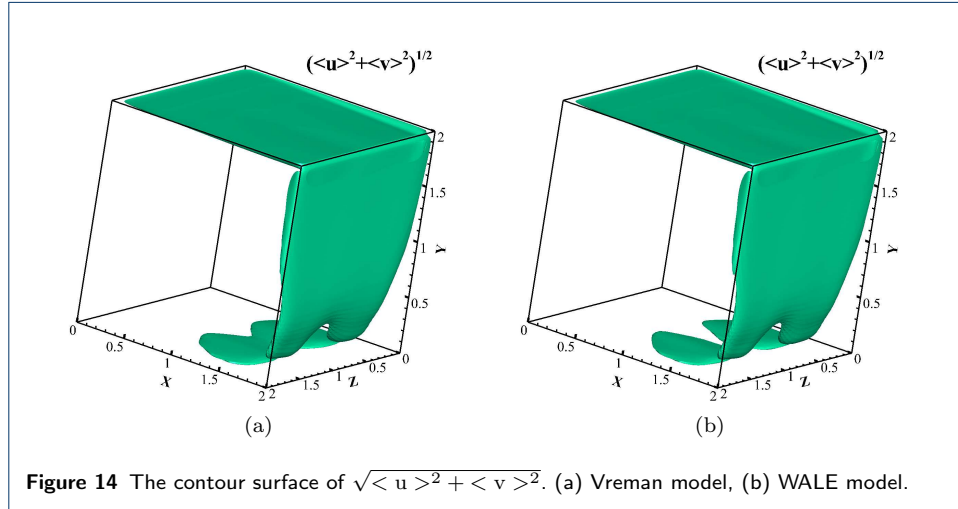


Figure 14 The contour surface of $\sqrt{< u >^2 + < v >^2}$. (a) Vreman model, (b) WALE model.

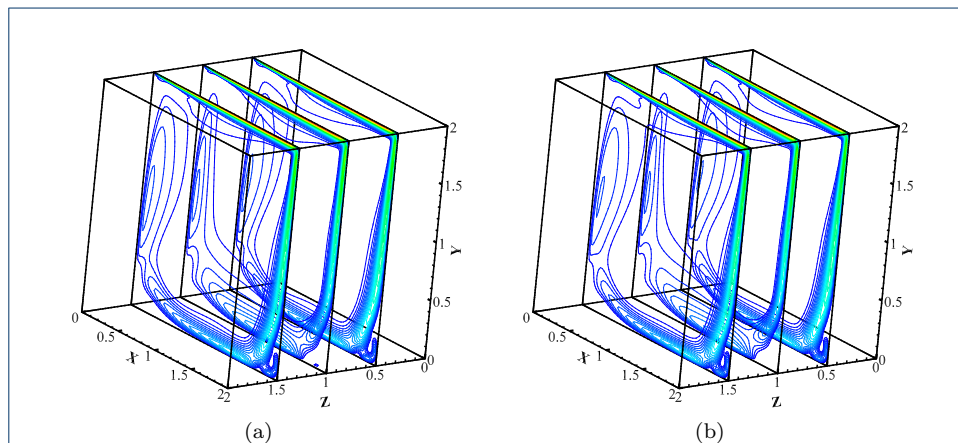


Figure 15 Distribution of $\sqrt{< u >^2 + < v >^2}$ on the planes $Z = 0.5$, $Z = 1.0$ and $Z = 1.5$. The contour range is $0.01 - 0.13$ with 50 levels. (a) Vreman model, (b) WALE model.

